

# Thermodynamics of Cation Binding to the Sarcoendoplasmic Reticulum Calcium ATPase Pump and Impacts on Enzyme Function

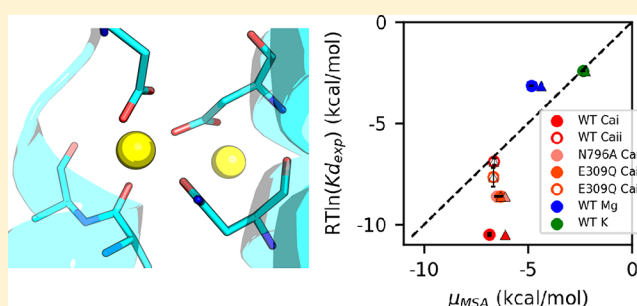
Bin Sun,<sup>†</sup> Bradley D. Stewart,<sup>†</sup> Amir N. Kucharski,<sup>†</sup> and Peter M. Kekenos-Huskey<sup>\*,†,‡</sup>

<sup>†</sup>Department of Chemistry, University of Kentucky, 505 Rose Street, Chemistry-Physics Building, Lexington, Kentucky 40506, United States

<sup>‡</sup>Department of Chemical and Materials Engineering, University of Kentucky, 177 F. Paul Anderson Tower, Lexington, Kentucky 40506, United States

## Supporting Information

**ABSTRACT:** Sarcoendoplasmic reticulum Ca<sup>2+</sup>-ATPase (SERCA) is a transmembrane pump that plays an important role in transporting calcium into the sarcoplasmic reticulum (SR). While calcium (Ca<sup>2+</sup>) binds SERCA with micromolar affinity, magnesium (Mg<sup>2+</sup>) and potassium (K<sup>+</sup>) also compete with Ca<sup>2+</sup> binding. However, the molecular bases for these competing ions' influence on the SERCA function and the selectivity of the pump for Ca<sup>2+</sup> are not well-established. We therefore used *in silico* methods to resolve molecular determinants of cation binding in the canonical site I and II Ca<sup>2+</sup> binding sites via (1) triplicate molecular dynamics (MD) simulations of Mg<sup>2+</sup>, Ca<sup>2+</sup>, and K<sup>+</sup>-bound SERCA, (2) mean spherical approximation (MSA) theory to score the affinity and selectivity of cation binding to the MD-resolved structures, and (3) state models of SERCA turnover informed from MSA-derived affinity data. Our key findings are that (a) coordination at sites I and II is optimized for Ca<sup>2+</sup> and to a lesser extent for Mg<sup>2+</sup> and K<sup>+</sup>, as determined by MD-derived cation–amino acid oxygen and bound water configurations, (b) the impaired coordination and high desolvation cost for Mg<sup>2+</sup> precludes favorable Mg<sup>2+</sup> binding relative to Ca<sup>2+</sup>, while K<sup>+</sup> has limited capacity to bind site I, and (c) Mg<sup>2+</sup> most likely acts as inhibitor and K<sup>+</sup> as intermediate in SERCA's reaction cycle, based on a best-fit state model of SERCA turnover. These findings provide a quantitative basis for SERCA function that leverages molecular-scale thermodynamic data and rationalizes enzyme activity across broad ranges of K<sup>+</sup>, Ca<sup>2+</sup>, and Mg<sup>2+</sup> concentrations.



## 1. INTRODUCTION

Sarcoendoplasmic reticulum Ca<sup>2+</sup>-ATPase (SERCA) is a 110-kDa transmembrane cation pump that actively transports Ca<sup>2+</sup> ions into the SR by utilizing energy released from adenosine triphosphate (ATP) hydrolysis (Figure 1).<sup>1</sup> SERCA has been widely studied for its role in returning intracellular Ca<sup>2+</sup> to basal levels following stimuli that elevate Ca<sup>2+</sup> content.<sup>2</sup> The pump's catalytic cycle is roughly characterized by four states comprising a sequential cycle E1 → E1P.2Ca → E2P.2Ca → E2. In E1, the Ca<sup>2+</sup> binding sites are exposed to the cytosolic space, whereas the E2 conformations expose the low-affinity Ca<sup>2+</sup> sites toward the SR lumen. The transition between E1 and E2 is driven by ATP hydrolysis at residue Asp 351<sup>1</sup> following Ca<sup>2+</sup> binding, for which E1P and E2P are the respective phosphorylated states of the enzyme. Accompanying transitions between catalytic states are prominent changes in its 10 transmembrane domain (TM) helices as well as the cytosolic actuator (A) domain, nucleotide-binding domain (N), and phosphorylation domain (P). Many of these changes have been resolved through X-ray crystallography.<sup>3–6</sup>

Based on available structural models of the protein and a wealth of biochemical studies,<sup>7–14</sup> reaction schemes linking the E1 and E2 states are beginning to emerge. Utilizing SERCA

vesicles coupled with spin label molecules, Inesi et al. observed a changed electron spin resonance spectrum upon Ca<sup>2+</sup> binding that revealed conformational changes in the enzyme.<sup>11</sup> Dupont and co-workers similarly measured changes in intrinsic fluorescence upon Ca<sup>2+</sup> binding and proposed a two-step Ca<sup>2+</sup> binding process to high affinity sites evidenced by slow fluorescence changes.<sup>9,10</sup> Additionally, conformational changes linking the E1 and E2 states were explored by kinetic studies of intrinsic fluorescence changes upon Ca<sup>2+</sup> binding and release.<sup>7,8</sup> An E309Q variant bound with two Ca<sup>2+</sup> in its phosphorylated state was determined via X-ray crystallography,<sup>15</sup> which revealed that altered TM arrangements caused by the mutation leads to impaired pump function. With respect to cation binding affinities, Inesi et al. measured Ca<sup>2+</sup> binding and stoichiometry to SERCA vesicles via chromatography,<sup>16</sup> while others have probed the binding of the noncognate Mg<sup>2+</sup> and K<sup>+</sup> ions via intrinsic fluorescence.<sup>17,18</sup>

In complement to experiment, extensive molecular dynamics simulations have uncovered many aspects of cation binding and SERCA function that are difficult to probe via

Received: December 31, 2018

Published: February 26, 2019

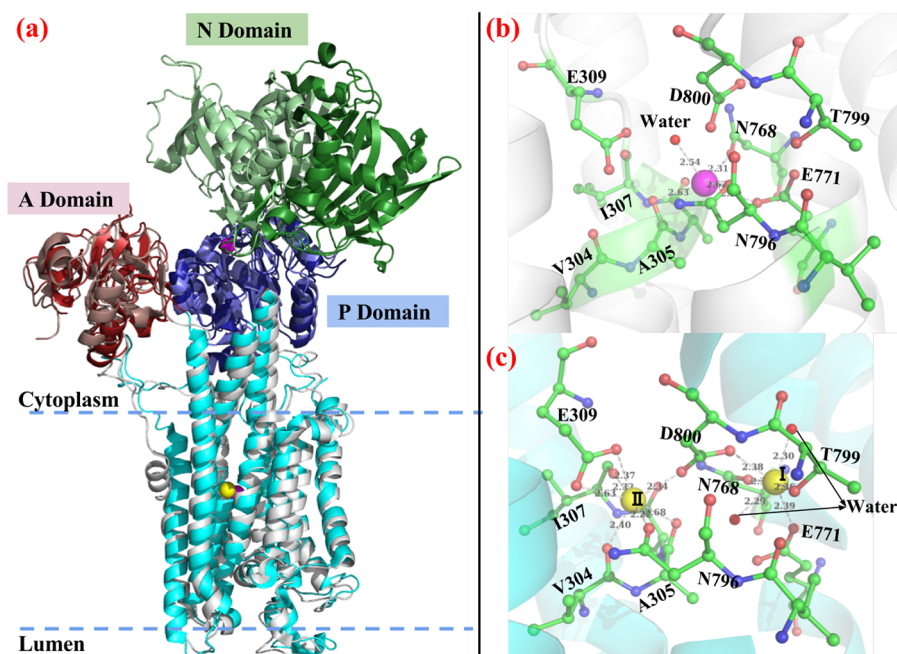


**Figure 1.** Comparison of  $\text{Ca}^{2+}$ -bound (PDB ID: 1su4) and  $\text{Mg}^{2+}$ -bound (PDB ID: 3w5b) SERCA crystal structures. (a) Superimposition of two crystal structures with 1su4/3w5b cytosolic domains (A, P, and N) colored in red/salmon, blue/slate, and green/pale green. The TM helices are colored in cyan and gray for 1su4 and 3w5b, respectively. (b, c)  $\text{Mg}^{2+}$  and  $\text{Ca}^{2+}$  binding site comparison. In this orientation, sites I and II are right and left, respectively.  $\text{Mg}^{2+}$  and  $\text{Ca}^{2+}$  are represented as magenta and yellow balls. The distance between coordination oxygen atoms and cations are also shown. The oxygen atoms of crystal water molecules are shown as red balls.

experimental approaches. Huang et al. first explored the  $\text{Ca}^{2+}$  binding pathways to SERCA TM sites via MD simulation and observed the cooperative binding of two  $\text{Ca}^{2+}$  ions.<sup>19</sup> Kekeneshuskey et al. performed MD simulations on SERCA with and in the absence of  $\text{Ca}^{2+}$  to examine gating of  $\text{Ca}^{2+}$  binding by residue E309,<sup>20</sup> in addition to estimating ion binding free energies and kinetics. Espinoza-Fonseca et al. evaluated the interaction energy between  $\text{Ca}^{2+}/\text{Mg}^{2+}/\text{K}^{+}$  and SERCA binding sites based on MD trajectories and reported that  $\text{Ca}^{2+}$  has the most negative (favorable) interaction energy while  $\text{K}^{+}$  has the least negative value.<sup>21</sup> In addition to these initial studies on cation binding to the SERCA pump, more recent studies have probed mechanisms of SERCA function and its modulation by regulatory proteins and drugs.<sup>22–29</sup>

Although studies have been reported on the roles of  $\text{Mg}^{2+}$  and  $\text{K}^{+}$  on SERCA binding, less has been done to provide a thermodynamic basis for their effects on SERCA function. This is of particular importance, as intracellular  $\text{K}^{+}$  and  $\text{Mg}^{2+}$  concentrations are orders of magnitude larger than the roughly sub-micromolar  $\text{Ca}^{2+}$  concentrations found in typical cells. Here, simulation studies of cation binding to molecular sites that resemble high affinity, amino acid-based motifs have been informative. Dudev et al. for instance constructed cation binding sites using model compounds and calculated cation binding energies via quantum mechanics.<sup>30</sup> Yu et al. designed a theoretical framework in combination with MD simulations to calculate cation binding free energies and assess geometric and confinement contributions.<sup>31</sup> Implicit models that describe  $\text{Ca}^{2+}$  binding thermodynamics as via ion density-based formalisms have also been reported, including reference interaction site modeling<sup>32</sup> and density functional theory.<sup>33</sup> Besides these methods relying on explicit binding site configurations, Nonner et al. developed the MSA model in which the binding site is treated as confined filter filled with

coordination oxygens. This variant of density functional theory has been used in rank-ordering the binding of cationic species to oxygen-rich binding domains such as EF-hands in  $\beta$  parvalbumin ( $\beta$ -PV)<sup>34</sup> and  $\text{Ca}^{2+}$  channel selectivity filters,<sup>35,36</sup> through describing the electrostatics and hard-sphere contributions to the chemical potential of partitioning ions into oxygen-rich “filters”.

Our study focused on utilizing (MD) derived data with thermodynamic and state-based models to assess contributions of  $\text{Mg}^{2+}$  and  $\text{K}^{+}$  binding on the SERCA turnover rate. Here we performed MD simulations of  $\text{Ca}^{2+}$ ,  $\text{Mg}^{2+}$ , and  $\text{K}^{+}$ -bound wild-type (WT) SERCA as well as the E309Q and N796A variants. These MD data provided structural information to assess cation binding thermodynamics via MSA to elucidate the molecular basis of SERCA’s preference of  $\text{Ca}^{2+}$  over  $\text{Mg}^{2+}$  and  $\text{K}^{+}$ . Further, we relate these studies of the E1 state ion binding to a state-based kinetic model of SERCA pump rate to determine the extents to which  $\text{Mg}^{2+}$  and  $\text{K}^{+}$  facilitate or inhibit catalysis. With this approach, we provide a multiscale and molecular basis for cation binding to SERCA and impacts on pump function.

## 2. RESULTS

We performed triplicate simulations of wild-type SERCA and its variants E309Q and N768A to probe the binding site coordination of the cations  $\text{Ca}^{2+}$ ,  $\text{Mg}^{2+}$ , and  $\text{K}^{+}$ , and each replica was at least 100 ns in length.  $\text{Ca}^{2+}$ - and  $\text{Mg}^{2+}$ -bound configurations of the protein have been determined through X-ray crystallography, but to our knowledge, the binding of  $\text{K}^{+}$  to the  $\text{Ca}^{2+}$  binding domain has only been resolved via simulation.<sup>21</sup> In this study, we critically examine the protein atoms and waters that directly coordinate bound cations. To ensure that our simulations of the intact protein are consistent with prior studies of the enzyme, we briefly summarize

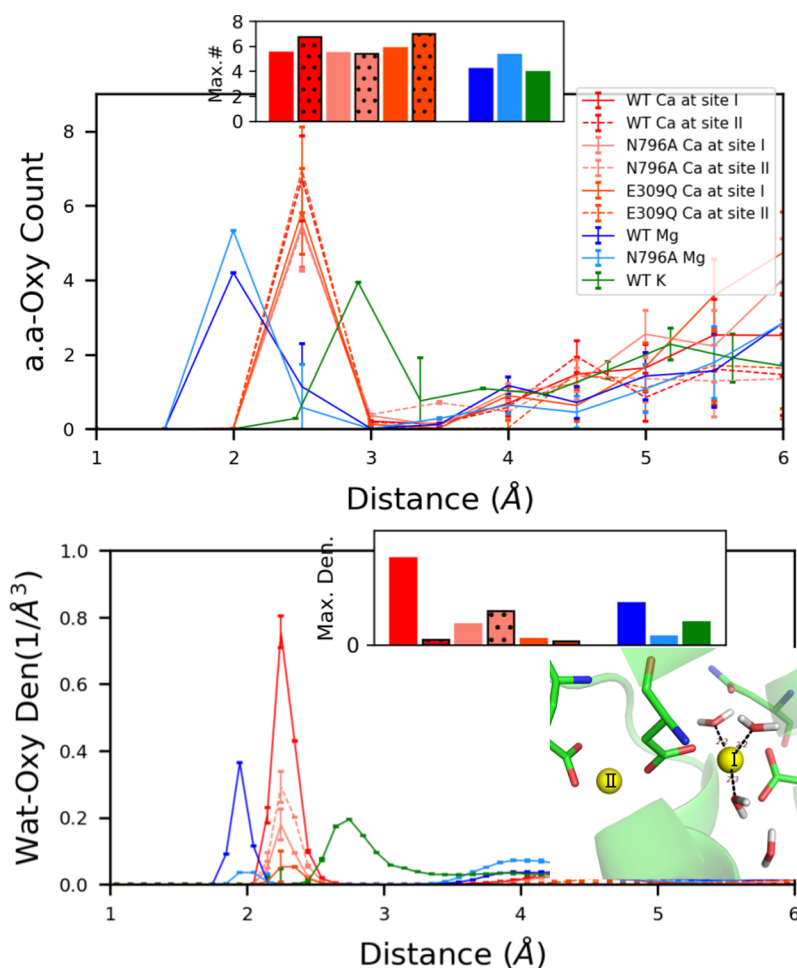


**Figure 2.** Radial distribution function (RDF) of amino acid and water oxygen atoms about bound  $\text{Ca}^{2+}$ ,  $\text{Mg}^{2+}$ , or  $\text{K}^+$ . The distribution around  $\text{Ca}^{2+}$  for each individual case is shown in Figure S9 for clarity. The inset bar graphs show the maximum number of coordinating amino acid oxygen and water density around the cation in each case (the bars with black dots represent site II  $\text{Ca}^{2+}$ ). The coordinating waters with site I  $\text{Ca}^{2+}$  of WT SERCA is also shown.  $\text{Ca}^{2+}$  ions bound to WT SERCA tend to reflect the highest degree of coordination among the modeled systems.

standard analyses of the transmembrane bundles and cytosolic domains in the Supporting Information (see Section S1.4).

### 2.1. Cation Coordination in the $\text{Ca}^{2+}$ Binding Region.

In this study, we highlight structural and dynamic contributions of the  $\text{Ca}^{2+}$  and  $\text{Mg}^{2+}$  binding domains to the thermodynamics of ion binding. This is analogous to our approach for probing  $\text{Ca}^{2+}/\text{Mg}^{2+}$ -binding to the  $\beta$  parvalbumin ( $\beta$ -PV) protein,<sup>34</sup> for which we used MD simulation-derived structural data from the cation-bound configurations to parametrize a statistical mechanical model called mean spherical approximation (MSA). Specifically, we used the radius of the ions' inner coordination sphere and amino acid oxygens comprising the sphere to estimate the binding site volume and coordinating oxygen density for MSA. We use a similar strategy for SERCA in that we assess the coordination of a given ion based on the number of oxygens within 6 Å of the bound ion. In contrast to our previous study, we additionally include coordinated waters in the MSA calculation that are directly involved in stabilizing the ion.

In Figure 2 we report radial distribution functions (RDFs) of cation-coordinating oxygens from the simulations. These RDFs demonstrate that  $\text{Ca}^{2+}$ ,  $\text{Mg}^{2+}$ , and  $\text{K}^+$  have varying degrees of coordination with amino acid oxygens within the binding site. We summarize the identity of the coordinating amino acids in Section S1.4, although from the perspective of MSA theory,

only the number of contributed amino acid oxygens is important. The  $\text{Ca}^{2+}$  within site I was optimally coordinated with 8.5 oxygens on average (including three water oxygens).  $\text{Ca}^{2+}$  within site II maintained six amino acid oxygen pairings, similar to the X-ray crystal structure, but did not directly coordinate waters. By virtue of having more coordinating oxygens, we speculate that the  $\text{Ca}^{2+}$  ion in site I is bound more tightly than that found within site II. In contrast, for the N796A variant, the site I  $\text{Ca}^{2+}$  had a reduced coordination number of six relative to over eight in the WT structure. Interestingly, for the site II  $\text{Ca}^{2+}$  in the N796A variant, the loss of coordination to residue 796 was compensated by interactions formed with E58 and a bound water molecule (see Figure S11b) to yield a greater coordination number than observed in the WT. For the E309Q variant, two possible side chain rotamers of Q309 were investigated, as both rotamers were viable starting positions (see Figure S11c,d for illustration of rotamer directions). We found that these rotamers yielded identical  $\text{Ca}^{2+}$  coordination patterns for the two binding sites: site I had six coordinating oxygens versus seven for site II, while neither included bound waters (see Figure S11c,d). Similar to the N796A site II  $\text{Ca}^{2+}$  case, E58 in TM1 also participated into the coordination with  $\text{Ca}^{2+}$  at site II in both rotamers of E309Q. Overall, these simulations reveal that ion/oxygen pairing is remarkably labile between site I and site II

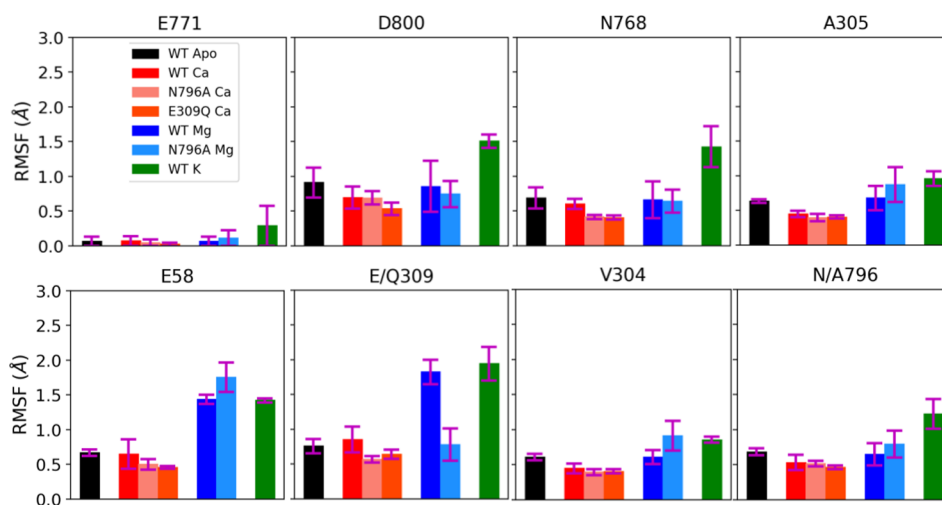


**Figure 3.** Heavy atom RMSF of key coordinating residues at the cation binding sites. The error bars were calculated from the triplicate trajectories for each case. The upper row represents site I residues while lower row displays site II residues (E58 was not involved in coordination with cations in the crystal structure, although interactions with bound ions were predicted in our simulations; see Figure S11).  $\text{Ca}^{2+}$ -bound configurations generally exhibit lesser mobility compared to the configurations with noncognate ions  $\text{Mg}^{2+}$  and  $\text{K}^+$ .

and can incorporate bound waters to maximize  $\text{Ca}^{2+}$  coordination.

In contrast to  $\text{Ca}^{2+}$ ,  $\text{Mg}^{2+}$  binds in a “hybrid” site between site I and site II with an average six coordinating oxygens (including one water molecule; see Figure S13a).  $\text{K}^+$ , on the other hand, binds site I with five coordinating oxygens (including one water molecule; see Figure S13c), while  $\text{K}^+$  at site II is highly dynamic and interchanges with water immobilized in the SERCA interior. Given that these ions are both positively charged and not remarkably different in size relative to  $\text{Ca}^{2+}$ , we had anticipated that the noncognate ions might adopt higher coordination numbers in the native  $\text{Ca}^{2+}$  sites, but the molecular simulations did not reflect this expectation; in Section 2.2 we provide a thermodynamic rationale via MSA theory for why these noncognate ions present impaired coordination numbers.

The differences in cation–oxygen coordination patterns for the cases considered are accompanied by variations in the coordinating residues’ mobilities relative to WT. These mobilities are measured as RMSF values in Figure 3, for which the upper row represents site I and the lower row, site II. Generally,  $\text{Ca}^{2+}$ -bound systems have RMSF values for most residues around 0.5 Å, which are the smallest among the ions considered. To a certain extent, the reduced mobility could be interpreted as an indication of tighter and more favorable binding, although this would come at an entropic cost that is not explicitly estimated here. We were, however, surprised to see little change in RMSF for the  $\text{Ca}^{2+}$ -free (apo) state versus the  $\text{Ca}^{2+}$ -bound cases. One possible reason is that, in the apo state, waters fill the binding sites and stabilize residues via a hydrogen bonding network (see Figure S7)—in this capacity, bound waters might “prop” open the  $\text{Ca}^{2+}$ -binding domains to promote rapid incorporation of solvated  $\text{Ca}^{2+}$  ions from the bulk medium. Additionally, we found that WT SERCA and its variants presented negligible differences in RMSF upon  $\text{Ca}^{2+}$  binding, whereas the noncognate  $\text{Mg}^{2+}$  and  $\text{K}^+$  manifest significant RMSF increases across all residues ( $\text{Mg}^{2+}$  generally above 0.8 Å and  $\text{K}^+$  above 1 Å). It is possible that the greater mobility of coordinating residues for the noncognate ions are indicative of impaired coordination. We had anticipated that

waters could be incorporated into the ions’ binding domain to suppress fluctuations in amino acids contributing to coordination, much as was observed for the apo state. However, it is apparent the strong electrostatic affinity for these ions with the coordination residues limited the volume within which waters could be incorporated. At a minimum, these data suggest that ion coordination is dynamic, with fluctuations on a nanosecond time scale (see Figure S6), which ultimately may play a role in selecting  $\text{Ca}^{2+}$  over noncognate ions.

## 2.2. Thermodynamics of Ion Binding at Sites I and II.

Molecular dynamics simulations provide qualitative insight into the binding of various ions in the binding sites of SERCA but alone do not directly predict affinities. Therefore, we explored MSA to semiquantitatively estimate free energies and selectivity of ion binding. MSA predicts chemical potentials of partitioning solvated ions into the SERCA binding domains from bulk solvent, assuming a similar approach that was performed for the  $\beta$ -PV<sup>34</sup> protein. Namely, MSA theory estimates the chemical potential of ion binding, based on the assumption of finite sized ions and chelating oxygens confined to a spherical binding site volume. To utilize this method, we first compute oxygen RDFs about bound ions. These data provide oxygen filter densities and volumes, from which chemical potentials of ion partitioning into the binding site “filter” from the surrounding bulk solution can be estimated. As shown in Figure 4,  $\text{Ca}^{2+}$  at site I of the WT case presents the most negative and therefore thermodynamically favorable MSA-predicted chemical potentials across all cases, corresponding to the largest number of coordination oxygens. For the SERCA variants, site I and site II  $\text{Ca}^{2+}$  ions have modestly less favorable chemical potentials compared with site I  $\text{Ca}^{2+}$  from WT cases, as the relative values were approximately 0.3 kcal/mol higher. These are consistent with the comparable  $\text{Ca}^{2+}$  coordination numbers present among the variants. Compared with  $\text{Ca}^{2+}$ -binding,  $\text{Mg}^{2+}$  binding at WT and variant SERCA yielded more significantly disfavored chemical potentials at approximately 2 kcal/mol relative to WT site I  $\text{Ca}^{2+}$ . Among all cases, the  $\text{K}^+$  relative potential was the most positive at 4.2 kcal/mol, indicating that  $\text{K}^+$  is the least thermodynamically favored at TM sites. For  $\text{Mg}^{2+}$  and  $\text{K}^+$ , the

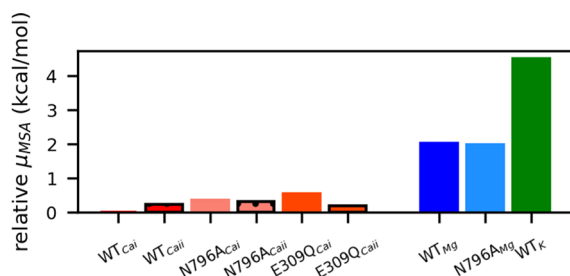


**Figure 4.** Mean spherical approximation (MSA)-predicted chemical potentials for each cation based on oxygen-coordination pattern (waters included) and optimal filter volumes derived from MD simulations. Potentials are given relative to  $\text{Ca}^{2+}$  bound to wild-type SERCA at site I.  $\text{Ca}^{2+}$  bound cases exhibit more favorable binding interactions compared to the binding of noncognate ions, with the WT cases reflecting the most favorable potentials relative to the N796A and E309Q variants.

MSA predicted potentials also correlated with the cation-coordination patterns as these two ions had reduced coordination number when compared with  $\text{Ca}^{2+}$  (5.2/4.7 for  $\text{Mg}^{2+}/\text{K}^+$  versus 8.5 for site I  $\text{Ca}^{2+}$ ). These data show that MSA could capture the key factors governing cation affinities such as coordination number and binding site volume. In addition, with inclusion of coordinating waters in MSA, the predicted potential for WT site I  $\text{Ca}^{2+}$  is most favorable among all cases, which agrees with experimentally measured affinities. Our MSA results indicate that site I confers greater  $\text{Ca}^{2+}$  affinity due to extensive inclusion of water coordination. In Section S1.4, we utilized the Grid Inhomogeneous Solvation Method (GIST) to assess the relative thermodynamics of water binding to the  $\text{Ca}^{2+}$  binding domain. In general, we found that when bound waters are present in the ions' coordination shells, the predicted free energies are on the order of  $-12$  kcal/mol and thus thermodynamically favorable.

The membrane into which SERCA is embedded presents a negative surface charge owing to solvent-exposed phosphate head groups.<sup>37</sup> The corresponding negative electrical potential can attract positively charged ions and thereby increase their concentration near the transmembrane-bound SERCA, as we previously observed in ref 20. Since the partitioning of cations into the SERCA binding sites depends on the composition of the surrounding electrolyte, we speculated that the local elevation of cations near the membrane surface would subsequently increase the concentration of bound cations. Additionally, the higher ionic strength could also reduce the desolvation energy and thereby further favor cation binding to SERCA, though this effect would likely be offset by screening electrostatic interactions between the cations and the oxygens in the SERCA  $\text{Ca}^{2+}$  binding domains. To investigate this hypothesis, we determined the effective ion concentration near the membrane using a 1D solution of the linearized Poisson–Boltzmann equation,<sup>38</sup>  $[i]_{\text{eff}} = e^{-\beta Z_i \zeta} [i]_{\text{bath}}$  where  $Z_i$  is the charge of ion and  $\beta = \frac{1}{k_B T}$ ,  $[i]_{\text{bath}}$  is ion concentration in the bath and  $\zeta$  is the membrane potential.

Assuming  $\zeta = -25$  mV,<sup>39</sup> we predicted that monovalent cation concentrations would be increased by 2.7-fold, anions would decrease by 0.37-fold, and the divalent  $\text{Ca}^{2+}/\text{Mg}^{2+}$  ions would increase by 7.4-fold. As shown in Figure 5, at low bath  $[\text{Ca}]$ , both  $\text{Mg}^{2+}$  and  $\text{K}^+$  were present in the SERCA  $\text{Ca}^{2+}$  binding domain with concentrations of 7.7 and 1.7 M, respectively. As bath  $[\text{Ca}]$  was increased,  $\text{Ca}^{2+}$  partitioned

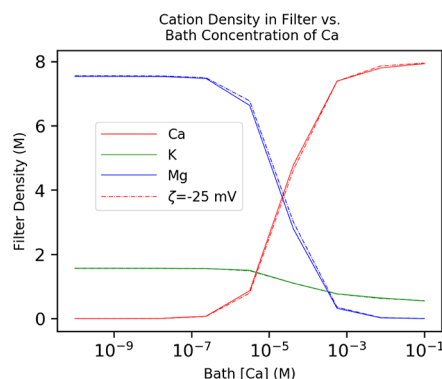


**Figure 5.** Cation concentration in the SERCA binding domains (assuming a filter volume =  $0.33 \text{ nm}^3$  from our MD simulations),  $N_{\text{oxy}} = 7$  (coordination number of  $\text{Ca}^{2+}$ ,<sup>30</sup> this value lies between the coordination number of site I,  $N_{\text{oxy}} = 8.5$ , and site II,  $N_{\text{oxy}} = 6.7$ , for  $\text{Ca}^{2+}$  determined in our simulation of WT SERCA) and with the cation solvation energy from ref 33.  $[\text{KCl}] = 150 \text{ mM}$  and  $[\text{MgCl}_2] = 2 \text{ mM}$ . As cytosolic  $\text{Ca}^{2+}$  is increased, and  $\text{Ca}^{2+}$  displaces  $\text{Mg}^{2+}$  bound to SERCA and reaches saturation at millimolar  $\text{Ca}^{2+}$  concentrations. Data are also presented assuming a membrane potential of  $\zeta = -25$  mV, which locally increases bath cation concentrations by several fold according to Poisson–Boltzmann theory estimates.

into the binding domain in favor of  $\text{Mg}^{2+}$ ; at roughly  $2 \times 10^{-5}$  M, the ratio of  $\text{Mg}^{2+}$  to  $\text{Ca}^{2+}$  was 1:1. The  $\text{Ca}^{2+}$  concentration at which  $\text{Mg}^{2+}/\text{Ca}^{2+}$  was 1:1 varied by roughly 0.6-fold under the assumption of charged versus neutral membrane. In other words, according to our model, the local electrostatic environment about the membrane did not significantly impact the  $\text{Ca}^{2+}$  binding affinity. In contrast, in ref 20 we demonstrated that the negative surface charge densities of SERCA and the lipid enhanced the association rate of  $\text{Ca}^{2+}$  to the protein, and thus the local electrostatic environment may have a greater contribution to ion binding kinetics than steady-state binding.

**2.3. Steady-State Catalytic Activity.** Lastly, we relate our predictions of  $\text{Ca}^{2+}$  and noncognate ion binding to the SERCA pumping rate. For the complete pumping cycle, two  $\text{Ca}^{2+}$  ions in the cytoplasm are transported into the SR by first binding SERCA to its E1 state. This binding process was proposed by Inesi et al.<sup>40</sup> to consist of two  $\text{Ca}^{2+}$  successive binding events via a cooperative mechanism. Subsequent steps include binding of MgATP, a slow conformational transition to the E2 state, release of  $\text{Ca}^{2+}$  ions into the SR lumen, and a return to the E1 apo state. In practice, by accounting for the transition rates between SERCA conformational states, the time-evolution of each state can be described, which in turn can be related to the pump's cycling rate. However, generally the transitions between the “micro” state conformations within the E1 or E2 “macro” states, such as the  $\text{Ca}^{2+}$  binding steps in E1, are rapid relative to the slow E1 to E2 transitions. Hence, the micro states comprising the E1 and E2 stages are approximately in steady-state. This allowed us to describe the SERCA pump cycle rate as a two-state model for the E1 and the E2 macro states (eq 8), which we used to relate experimentally and computation-determined binding constants to SERCA function.

In this state-based model, with exception to the undetermined transition rates between E1 and E2 ( $k_5^+$ ,  $k_5^-$ ,  $k_6^+$ , and  $k_6^-$ ), the resting rate constants and substrate concentrations were taken from refs 40 and 41. The above unknown rates

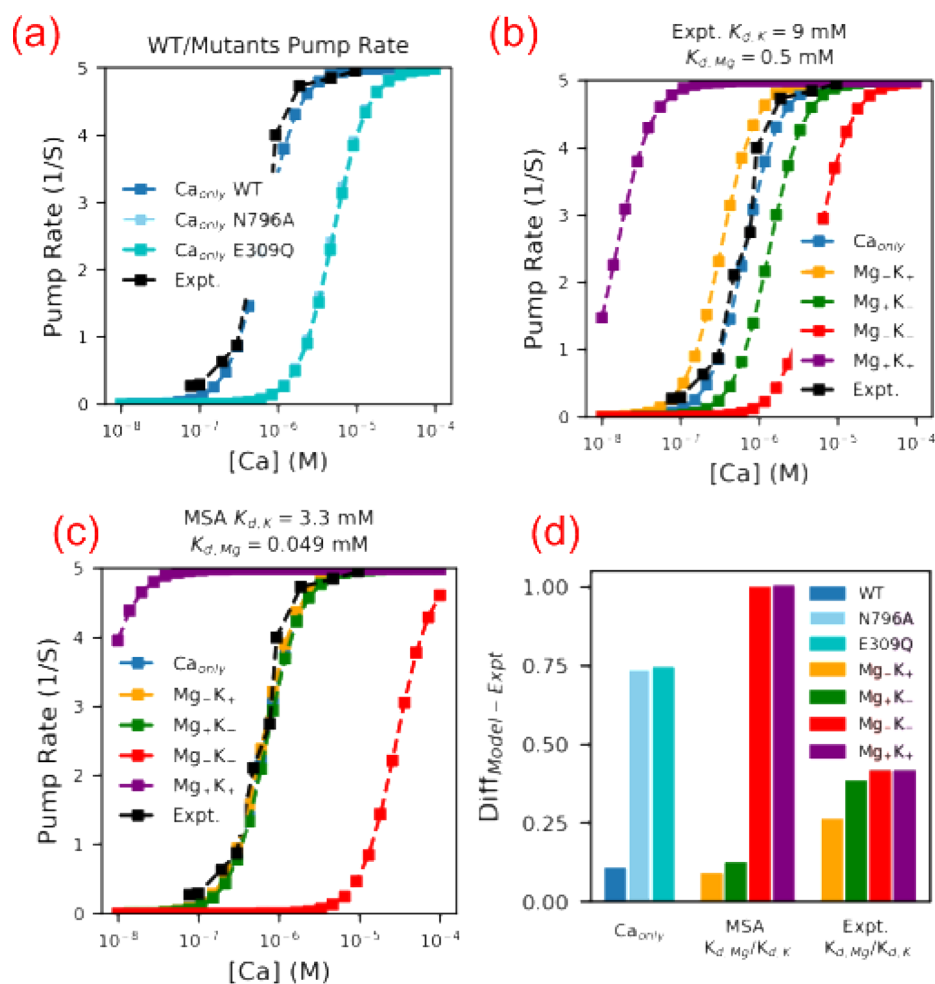


**Figure 6.** (a) Comparison of pump turnover rate between WT and SERCA variants using the  $\text{Ca}_{\text{only}}$  model with MSA predicted  $\text{Ca}^{2+}$  affinity for N796A and E309Q variants. The experimental data is from Inesi et al.<sup>40</sup> (b, c) Comparison of SERCA pump turnover rate of different state models against experimental data at  $[\text{Mg}] = 2 \text{ mM}$  and  $[\text{K}] = 150 \text{ mM}$ . In panel (b) the experimentally measured  $K_{d,K}$  and  $K_{d,\text{Mg}}$  in Table S4 were used. In panel (c) the MSA predicted  $K_{d,K}$  and  $K_{d,\text{Mg}}$  were used. (d) Normalized difference between each state model and experimental data for panels (a)–(c), as evaluated by eq 1. Our state-based models reproduce steady-state WT SERCA pumping rates and predict impaired rates for the N796A and E309Q variants.

were left as free parameters that were fitted to reproduce experimentally determined turnover rates from ref 40 (see black data points in Figure 6a).

This fitting accuracy was assessed as the difference between model predicted rates, and experimental values reached minimum, as defined by

$$\text{Diff} \equiv \sqrt{\left( \frac{\sum_{i=1}^N (M_{r,i} - \text{Expt}_{r,i})^2}{N} \right)} \quad (1)$$

where  $M_{r,i}$  is the state model predicted pump rate at experimental  $[\text{Ca}]$ ,  $\text{Expt}_{r,i}$  is the experimentally measured rate, and  $N$  is the total number of data points. As shown in Figure 6a, the fitted  $\text{Ca}_{\text{only}}$  model (blue) reproduces the experimentally determined SERCA turnover rates as a function of cytosolic  $\text{Ca}^{2+}$  concentration, which validates our state-based model.

**2.4. Effects of Noncognate Ions on Steady-State Behavior of SERCA.** Since a primary focus of this study was to elucidate to which extent the noncognate ions  $\text{Mg}^{2+}$  and  $\text{K}^+$  influenced the SERCA transport cycle, we introduced additional microstates representing the  $\text{Mg}^{2+}$ - and  $\text{K}^+$ -bound

configurations. The resulting representations are summarized in Figure S4 and differ in terms of whether the ions serve as inhibitors or intermediates. Using the fitted model from Figure 6a, we introduced dissociation constants for the  $\text{Mg}^{2+}$  and  $\text{K}^+$  species. We considered two strategies for defining those constants: (1) using experimentally determined values from Tables S4 and (2) constants determined from rescaling of the MSA-predicted values. For (2), the MSA predicted  $\text{Mg}^{2+}/\text{K}^+$  chemical potentials were first converted to dissociation constants via  $K_d = e^{\mu_{\text{MSA}}/RT}$ . Second, the  $K_d$  values were multiplied by a scaling factor,  $\lambda$ , that minimizes the difference between the MSA-predicted and experimentally measured  $\text{Ca}^{2+}$  dissociation constants,

$$(\text{Cai}_{\text{ref}} - \lambda \cdot \text{Cai}_{\text{MSA}})^2 - (\text{Caii}_{\text{ref}} - \lambda \cdot \text{Caii}_{\text{MSA}})^2 = 0 \quad (2)$$

where  $\text{Cai}_{\text{ref}}/\text{Caii}_{\text{ref}}$  and  $\text{Cai}_{\text{MSA}}/\text{Caii}_{\text{MSA}}$  are site I/II  $\text{Ca}^{2+}$  dissociation constants from ref 40 ( $4 \times 10^{-8} \text{ M}$  and  $4 \times 10^{-6} \text{ M}$ ) and from MSA calculations ( $9.55 \times 10^{-6} \text{ M}$  and  $1.38 \times 10^{-5} \text{ M}$ ), respectively. Equation 2 was minimized by  $\lambda = 0.17$ , thus yielding  $4.93 \times 10^{-5} \text{ M}$  and  $3.3 \times 10^{-3} \text{ M}$  for the MSA-predicted values of  $K_{d,\text{Mg}}$  and  $K_{d,K}$  for  $\text{Mg}^{2+}$  and  $\text{K}^+$  (see also Table S3). Predictions of the SERCA cycling rate using

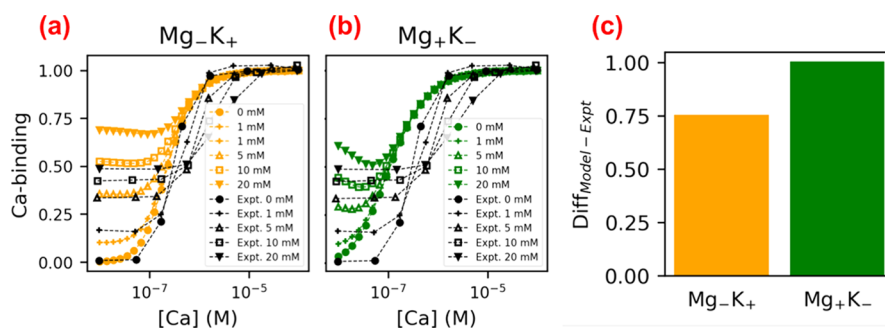


**Figure 7.** (a, b) Comparison of [Ca] dependence of Ca<sup>2+</sup>-SERCA binding of Mg<sub>-</sub>K<sub>+</sub> and Mg<sub>+</sub>K<sub>-</sub> models at varying Mg<sup>2+</sup> concentrations ([K] = 150 mM) against experimental data from ref 17. Experimentally measured  $K_{d,K}$  and  $K_{d,Mg}$  were used. (c) Normalized difference between state models and experimental data as evaluated by eq 1. The Mg<sub>-</sub>K<sub>+</sub> model, which assumes Mg<sup>2+</sup> and K<sup>+</sup> act as inhibitors and agonists, respectively, provides the best fit to experimental data.

experimentally determined dissociation constants are shown in Figure 6b and the rescaled MSA constants in panel (c). Both approaches indicate that the Mg<sub>+</sub>K<sub>-</sub> (green) and Mg<sub>-</sub>K<sub>+</sub> (yellow) provide the best agreement with the experimentally measured turnover rates, as these two models have relatively smaller normalized difference values than other models, with the MSA-determined dissociation constants yielding the strongest agreement overall. Hence, the cycling rate data reported by Cantilina et al.<sup>40</sup> was sufficient to eliminate two of the four proposed models.

To discriminate between the remaining Mg<sub>+</sub>K<sub>-</sub> and Mg<sub>-</sub>K<sub>+</sub> models, we next assessed the abilities of the respective models to reproduce steady-state Ca<sup>2+</sup> binding data measured at various Mg<sup>2+</sup> concentrations by Guillain et al.<sup>17</sup> In these experiments, both the E1.Mg and the E1.2Ca states contributed a fluorescence signal indicative of Ca<sup>2+</sup> saturation; therefore, we report in Figure 7 the combined probabilities of those states,

$$P_{\text{Cabinding}} = P_{\text{E1.Mg}} + P_{\text{E1.2Ca}} \quad (3)$$

where  $P_{\text{E1.Mg}}$  and  $P_{\text{E1.2Ca}}$  are the probabilities of the E1.Mg and E1.2Ca states (see Section S1.3). The experimental data (black) shown in Figure 7 demonstrate that Ca<sup>2+</sup> saturation naturally increases with increasing cytosolic Ca<sup>2+</sup>, but importantly, saturation increases as Mg<sup>2+</sup> is raised from 0 mM (circles) to 20 mM (solid triangles). These data indicate that Mg<sup>2+</sup> locks SERCA into an E1 state in absence of Ca<sup>2+</sup>. We plot in Figure 7a,b the predicted  $P_{\text{Cabinding}}$  data for the Mg<sub>-</sub>K<sub>+</sub> and Mg<sub>+</sub>K<sub>-</sub>, respectively, as well as the fit in Figure 7c. We find that the Mg<sub>-</sub>K<sub>+</sub> model provides the optimal fit with difference of 0.75 normalized to the Mg<sub>+</sub>K<sub>-</sub> model. The Mg<sub>-</sub>K<sub>+</sub> model correctly captures the plateau in Ca<sup>2+</sup> saturation at Ca<sup>2+</sup> concentrations below  $1 \times 10^{-7}$ , in contrast to the competing model. We note that as Mg<sup>2+</sup> is increased to unphysiologically high concentrations ( $\geq 5$  mM), the slope of the experimentally determined saturation curves decrease, which is indicative of a loss in Ca<sup>2+</sup>-binding cooperativity. Our model does not directly consider ion-dependent modulation of Ca<sup>2+</sup> binding cooperativity; therefore, this behavior is not reproduced in our predicted data and accounts for some of the error relative to experiment. Additionally, we predict a greater population of the Ca<sup>2+</sup>-bound state at increasing Mg<sup>2+</sup> levels than is experimentally observed, which accounts for the remainder of the error. Nevertheless, we find that Mg<sub>-</sub>K<sub>+</sub> model provides the best agreement with experimental data, especially within physiological Mg<sup>2+</sup> concentrations. Therefore,

Mg<sup>2+</sup> most likely acts as inhibitor and K<sup>+</sup> as an intermediate in the SERCA pumping cycle.

Lastly, as a demonstration of how MSA-predicted Ca<sup>2+</sup> affinities could be applied to infer changes in SERCA pumping function, we compared the turnover rates between WT and two variants using relative affinity estimates from Section 2.2. To be consistent with the procedure of obtaining Mg<sup>2+</sup>/K<sup>+</sup> affinity from the MSA potentials, the same scaling factor  $\lambda = 0.17$  was applied to the MSA-predicted affinities for the E309Q and N796A variants (Ca<sup>2+</sup> affinities at site I/II are  $2.98 \times 10^{-6}$  M/ $2.81 \times 10^{-6}$  M for N796A and  $4.06 \times 10^{-6}$  M/ $2.25 \times 10^{-6}$  M for E309Q). Relative to WT SERCA for which the half-maximal pump rate (approximately 2.5 per second) occurs at  $6 \times 10^{-7}$  M[Ca], the weaker affinities exhibited by the E309Q and N796A variants right-shift the half-maximal rate to  $\sim 1 \times 10^{-5}$  M[Ca]. In other words, the SERCA variants are essentially nonfunctional within physiological Ca<sup>2+</sup> concentrations ( $1 \times 10^{-7}$  to  $1 \times 10^{-6}$  M<sup>42</sup>), which is consistent with experimentally observed decreases in SERCA activity for the E309Q and N796A variants.<sup>43</sup> Although we recognize that the experimentally measured activities arise from a culmination of factors beyond just the Ca<sup>2+</sup> binding affinity in the binding domains, these data qualitatively indicate that MSA predicted affinities can then be used to rationalize steady-state pump turnover rates estimated from molecular-level simulations.

### 3. DISCUSSION

**3.1. Ion Coordination and Contributions to Cation Binding Affinity.** A key contribution from this study was our use of MSA theory to evaluate trends in Ca<sup>2+</sup> and noncognate binding in the SERCA E1 states. By using molecular dynamics simulations of the wild type and two site-directed mutations, we could probe shifts in the binding site configurations—relative to the available crystal structures of the pump—that contribute to chelating cations. Overall, the MSA theory, when informed using molecular simulation data including water distributions, appears to be effective in rank-ordering ions by affinity (approximately  $-7$  to  $-10$  kcal/mol, see Figure 8). Further, our state-based model of SERCA pumping function correctly captures cycling rates across physiological Ca<sup>2+</sup> concentrations and predicts functional effects of site-directed mutations (N796A and E309Q).

We first applied this combined MSA/MD technique to an EF-hand containing protein called  $\beta$  parvalbumin to investigate factors contributing to its Ca<sup>2+</sup> affinity and selectivity.<sup>34</sup> In both systems, the MSA/MD approach indicated that high

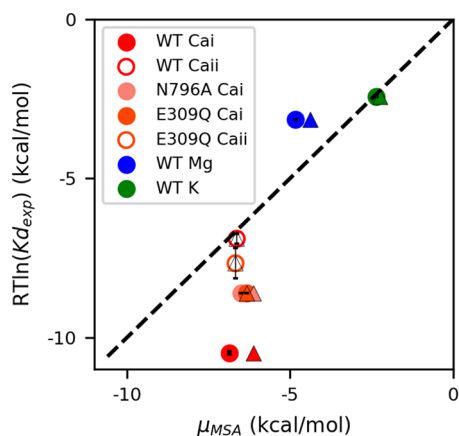


**Figure 8.** Correlation between MSA predicted chemical potential and experimentally measured binding free energy. The circles and triangles represent MSA results with waters and without waters taken into account, respectively.  $RT = 0.593$  kcal/mol at room temperature and  $K_{d,exp}$  is experimentally measured dissociation constants in Table S4. The MSA chemical potentials correctly rank-order  $\text{Ca}^{2+}$  versus noncognate ion binding.

affinity  $\text{Ca}^{2+}$  binding is afforded through the tight clustering of chelating oxygens with partial negative charges. Importantly, by predicting chemical potentials of ion binding, the MSA theory provided thermodynamic information about the relative competition between ions for the  $\text{Ca}^{2+}$  binding domains, which is generally unfeasible by MD alone. For instance, we determined that  $\text{Mg}^{2+}$ , and not  $\text{K}^+$ , is thermodynamically more probable to occupy the pump at low  $\text{Ca}^{2+}$  levels but is disfavored as  $\text{Ca}^{2+}$  rises toward micromolar concentrations typical in eukaryotic cells. In principle, this approach could additionally account for variations in electrolyte composition expected near charged lipid bilayers, but we found scant differences in binding assuming a surface charge of 25 mV (see Figure 5).

Consistent with our earlier findings for  $\text{Ca}^{2+}$ -binding to  $\beta$  parvalbumin,<sup>34</sup> MSA predicts increasing stability of the  $\text{Ca}^{2+}$  ion as the number of coordinating oxygens is increased. This

trend reversed as the oxygen density increased beyond roughly six per  $2.2 \times 10^{-1} \text{ nm}^3$ , which is presumably when the volume is insufficient to accommodate all coordinating oxygens. For the E309Q and N796A variants, we potentially reduced the number of oxygens that could directly coordinate  $\text{Ca}^{2+}$ . Based on the MD simulations for E309Q, however, it appeared that the loss of one carboxylic acid oxygen was compensated by a new interaction with E58 that maintained the same coordination number as the wild-type structure. This suggests that there is some degree of flexibility in coordination partners for the ion, which may facilitate the E309 residue's role in kinetically gating the binding site.<sup>20</sup> In contrast, the N796A mutation was not offset by a nearby available oxygen; thus, the predicted chemical potential was less favorable. Therefore, our data suggest that the MSA could reasonably rank-order  $\text{Ca}^{2+}$  binding stabilities based on structures of the immediate coordination shell based on Figure 4, but it is less sensitive to broad ranges of binding affinities reported in the literature (see Figure 8).

We note that our predictions of favorable binding stabilities for  $\text{Ca}^{2+}$  at site II for the N796A and E309Q variants are at odds with Inesi et al.,<sup>44,45</sup> who suggested based on SERCA ATPase activity that the site was incapable of binding  $\text{Ca}^{2+}$ . Surprisingly, a structure of the E309Q variant (PDB ID: 4nab<sup>15</sup>) deposited in the protein databank contains  $\text{Ca}^{2+}$  at both binding sites. Ostensibly, the E309Q variant has a much lower but nonzero affinity for  $\text{Ca}^{2+}$ . Thus, it is likely that the MSA model does not sufficiently penalize nonoptimal  $\text{Ca}^{2+}$  coordination or reflect changes in internal strain that might disfavor coordination.<sup>34</sup>

**Roles of Water in Facilitating Coordination.** We also found that including water distributions made a modest improvement in chemical potentials, as per Figure 8. Based on Figure S5, the narrow binding site volumes presented in sites I and II favor  $\text{Ca}^{2+}$  and  $\text{Mg}^{2+}$  over  $\text{K}^+$ , while both divalent ions are increasingly stabilized by greater densities of coordinating oxygens and waters. It is interesting that the water-free MSA calculations indicate  $\text{Ca}^{2+}$  could be more stable in a binding site volume of  $2.2 \times 10^{-1} \text{ nm}^3$ , which is smaller than the volume presented in the MD simulations, albeit with a fewer

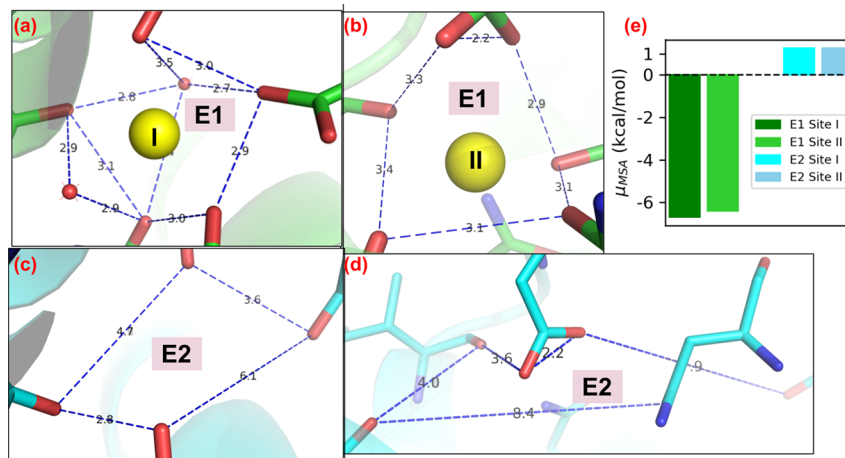


**Figure 9.** Comparison of  $\text{Ca}^{2+}$  binding sites in E1 state (a, b) and E2 state (c, d) from crystal structures of PDB 1su4 and 3b9b,<sup>6</sup> respectively.  $\text{Ca}^{2+}$  and water molecules are shown as yellow and red spheres, respectively. The blue dashed lines in (a) and (b) outline the overall shape of  $\text{Ca}^{2+}$  coordinating spheres in E1 state while in (c) and (d) they depict assumed  $\text{Ca}^{2+}$  binding sites in the E2 state. Panel (e) depicts MSA predicted  $\text{Ca}^{2+}$  chemical potential for these two sites. In the E1 state the number of coordinating oxygens are seven and six for sites I and II while these values are assumed as four for both sites in the E2 state.

number of oxygens (approximately five versus six). However, when water is considered, the stabilities at the smaller binding volumes are disfavored. It is possible that there is a kinetic advantage to having mobile waters involved in coordination, which could favor more rapid exchange of bound ions with the surrounding solvent. It is also possible that the trend can be explained on a thermodynamic basis; namely, that by preserving waters that coordinate in the ion in bulk solvent, the desolvation cost upon binding SERCA are reduced, which should increase the apparent binding affinity. An intriguing possibility is that the  $\text{Ca}^{2+}$  affinity could be indirectly tuned by controlling the density of binding site waters.

**$\text{Ca}^{2+}$  Dissociation during E2 Transition.** The primary function of the SERCA pump is to transport cytosolic  $\text{Ca}^{2+}$  into the sarcoplasmic or endoplasmic reticulum; therefore, we verified that MSA would indeed predict an unfavorable change in chemical potential based on conformational changes induced in sites I and II upon forming the E2 state. Since the focus of this study was on the E1  $\text{Ca}^{2+}$  binding thermodynamics, we did not perform MD simulations of the E2 state. Nevertheless, based on the crystal structure of SERCA/beryllium fluoride complex (PDB ID: 3b9b<sup>6</sup>), which represents the pump's E2P state, we illustrate in Figure 9 that changes in the  $\text{Ca}^{2+}$  binding site configuration culminate in a significant reduction in oxygens that could potentially coordinate  $\text{Ca}^{2+}$ . We further evaluate the binding stability for a hypothetical  $\text{Ca}^{2+}$  bound between the labeled coordination groups and find that the MSA values are not only more positive than those of the E1 state but are additionally greater than 0 kcal/mol. The positive values of approximately 1 kcal/mol indicate that  $\text{Ca}^{2+}$  binding at these positions is less thermodynamically favorable than partitioning into the surrounding bulk electrolyte. In other words, when SERCA transitions into the E2 state, it is thermodynamically preferred for  $\text{Ca}^{2+}$  to vacate the binding site in favor of the reticulum lumen. Along these lines, mutations that alter the free energy difference for the  $\text{Ca}^{2+}$  sites in the E1 and E2 configurations could affect the efficiency of the ATPase.

It has been suggested that the number of cations ( $\text{Ca}^{2+}$ ,  $\text{Mg}^{2+}$ , and  $\text{K}^+$ ) bound to SERCA is approximately constant across its many conformational states.<sup>46</sup> In other words,  $\text{Ca}^{2+}$  binding is offset by  $\text{Mg}^{2+}$  and  $\text{K}^+$  dissociation. ATP is bound to SERCA in complex with  $\text{Mg}^{2+}$ ,<sup>47</sup> but there also exists structural<sup>48</sup> and activity<sup>49</sup> data that confirm  $\text{Mg}^{2+}$  binds in the pump's transmembrane region. Toyoshima et al.,<sup>48</sup> for example, obtained the X-ray crystal structure of the pump with a single  $\text{Mg}^{2+}$  bound at a "hybrid" transmembrane site, for which the ion is coordinated by  $\sim 5$  oxygens with distances of approximately 2.0 Å. Since  $\text{Mg}^{2+}$  bears the same charge as  $\text{Ca}^{2+}$ , but with a modestly smaller radius, it is somewhat surprising that  $\text{Mg}^{2+}$  preferentially binds at an intermediate site between the canonical  $\text{Ca}^{2+}$  binding sites I and II. We attribute the thermodynamic preference for  $\text{Ca}^{2+}$  at those sites based on two factors: the higher desolvation energy for  $\text{Mg}^{2+}$  relative to  $\text{Ca}^{2+}$  (779.94 kT versus 648.65 kT<sup>33</sup>) and the smaller binding site volume for the intermediate site versus sites I and II. With respect to the latter factor, in principle,  $\text{Mg}^{2+}$  could reduce the site I and II volumes by pulling the chelating oxygens toward the smaller ion, as we previously observed in ref 34. For the EF-hand (helix–loop–helix) containing protein, we found that constricting the binding loop region introduced greater strain for  $\text{Mg}^{2+}$  relative to  $\text{Ca}^{2+}$ , which we suggested would reduce the overall binding affinity for  $\text{Mg}^{2+}$ . Although we did not

explicitly evaluate strain that could be introduced upon  $\text{Mg}^{2+}$ -binding for SERCA, we anticipate an even greater cost for reducing the binding site volume, since the chelating amino acids are firmly tethered to relatively immobile transmembrane helices. It is important to emphasize, though, that the nonoptimal volumes for  $\text{Mg}^{2+}$  binding at sites I and II does not preclude the ion from binding, as we demonstrate high binding probabilities at very low  $\text{Ca}^{2+}$  levels (see Figure 7).

Consistent with our earlier findings in  $\beta$  parvalbumin,  $\text{K}^+$  is disfavored from binding the native  $\text{Ca}^{2+}$  binding volume based on its significantly larger radius and smaller charge.<sup>50</sup> However,  $\text{K}^+$  and other monovalent cations have been demonstrated to stimulate SERCA function, with  $\text{K}^+$  being the most efficient agonist.<sup>18,46,49</sup> Moreover, based on molecular simulations performed in the presence of transmembrane-bound  $\text{K}^+$ , Espinosa-Fonseca et al. suggest that  $\text{K}^+$  facilitates the pump's E2 to E1 transition through its stabilization of the E1 state.<sup>21</sup> In our simulations, we found that of the two  $\text{K}^+$  ions placed in the  $\text{Ca}^{2+}$  binding domains, the site I  $\text{K}^+$  remained bound with approximately four coordinating oxygens with ion/oxygen distances exceeding 4 Å. Based on the MSA predictions, although  $\text{K}^+$  has a favorable ( $\mu < 0$ ) binding potential that is consistent with its submillimolar binding affinity at site I,<sup>18</sup>  $\text{Mg}^{2+}$  and  $\text{Ca}^{2+}$  are considerably more likely to be bound (see Figure 5). Meanwhile, water frequently exchanged with the  $\text{K}^+$  in site II, which is suggestive of a low affinity for the cation.

Based on our comparison with proteins that selectively bind  $\text{K}^+$ , such as the KcsA  $\text{K}^+$  channel, selective binding of  $\text{K}^+$  over competing  $\text{Ca}^{2+}$  might best be afforded through placement of carbonyl oxygens at sufficiently large distances to accommodate the  $\text{K}^+$  ion's larger volume. Namely, in  $\text{K}^+$  channels, oxygens from the backbone or side chains of amino acid forming the selectivity filter are exquisitely arranged to achieve precise pore size control and  $\text{K}^+$ –oxygen interaction strength.<sup>51</sup> In contrast, it is likely that  $\text{K}^+$  exerts its agonistic effects on SERCA through binding the cytoplasmic domain, as was evidenced in a crystal structure determined by Sørensen et al. based on a bound  $\text{K}^+$  ion in the P-domain.<sup>5</sup> According to the  $\text{K}^+$ –oxygen coordination pattern shown in Figure S10, the MSA predicted potential for the P domain  $\text{K}^+$  is  $-2.38$  kcal/mol, which is comparable to the values predicted for  $\text{K}^+$  bound to site I ( $-2.35$  kcal/mol). Consistent with this structural evidence, the E2P.2Ca dephosphorylation data indicate that  $\text{K}^+$  stimulates the  $\text{Ca}^{2+}$ -release step in this state, whereby the luminal  $\text{Ca}^{2+}$  affinity is reduced, rates of exchanging luminal  $\text{Ca}^{2+}$  with luminal solvated  $\text{Ca}^{2+}$  are accelerated,<sup>52</sup> and  $\text{Ca}^{2+}$  release is enhanced.<sup>53</sup> Similarly, dephosphorylation of the E2P state is blunted in the absence of  $\text{K}^+$ .<sup>46</sup>

Although the thermodynamics of  $\text{K}^+$  binding are unfavorable relative to  $\text{Mg}^{2+}$  and  $\text{Ca}^{2+}$ , there remains the possible role of  $\text{K}^+$  in shaping the kinetics of the SERCA function. It has been speculated, for instance, that  $\text{K}^+$  accelerates  $\text{Ca}^{2+}$  binding by first transiently occupying site I, after which it exchanges quickly with a  $\text{Ca}^{2+}$  at site II.<sup>53</sup>  $\text{K}^+$ -facilitated exchange could therefore permit faster incorporation of  $\text{Ca}^{2+}$  into site I, as opposed to the direct migration of  $\text{Ca}^{2+}$  into a site that is potentially only partially formed.<sup>53</sup> This interpretation is consistent with our observations from molecular dynamics simulations and was initially reported in simulations of  $\text{Ca}^{2+}$ -free SERCA by Musgaard et al.<sup>54</sup>

**3.2. Relating Cation Affinity to ATPase Activity.** In our opinion, the bridging of molecular-level simulation and MSA thermodynamic data with state-based models represents a

significant contribution toward multiscale modeling of steady-state SERCA activity. Numerical and computational modeling of SERCA activity has spanned phenomenological frameworks, such as Hill-type models<sup>55–57</sup> to those representing distinct stages of the catalytic process as states.<sup>40,41,58–60</sup> Our implementation is based on the stepwise binding of  $\text{Ca}^{2+}$  originally proposed by Inesi et al.<sup>40</sup> but additionally considers  $\text{Mg}^{2+}$ - and  $\text{K}^{+}$ -bound states, followed by a reduction scheme to consolidate E1 states separately from those comprising the E2 configurations. Significantly, the states defined in our model coincide with SERCA structures determined by X-ray crystallography and are ordered in a manner consistent with assays of the SERCA function.<sup>61</sup> In contrast, the state model proposed by Tran et al.<sup>41</sup> assumed that ATP binding precedes the binding of two  $\text{Ca}^{2+}$  ions, which has not been experimentally verified.

Existing models of the SERCA function have faithfully recapitulated the pump's activity. However, an advantage of our state-based model is that its alignment with experimentally determined structures permits us to directly investigate how structural modifications might impact activity. For example, we performed MSA/MD simulations of two mutated SERCA variants that yielded modified  $\text{Ca}^{2+}$  binding constants that we used to predict SERCA activity (see Figure 6). While we acknowledge that there are likely myriad changes to the pump's energetics following mutation that could be accounted for in the state-based model, our implementation here is a significant step toward structure-based modeling of SERCA activity. At a minimum, our fitted state model is consistent with steady-state pump rates data collected as a function of  $\text{Ca}^{2+}$  by Cantilina et al.<sup>40</sup> and  $\text{Ca}^{2+}$ -saturated versus  $\text{Mg}^{2+}$ ,<sup>17</sup> as well as molecular simulations that predict  $\text{Mg}^{2+}$  inhibition of the pump.<sup>21</sup> Furthermore, by considering different linkages of  $\text{K}^{+}$ - and  $\text{Mg}^{2+}$ -bound states to the reaction scheme, we were able to determine that assumptions of  $\text{Mg}^{2+}$  inhibition and  $\text{K}^{+}$  agonist were most consistent with experimental data collected by Guillain et al.<sup>17</sup> In principle, multiscale models of SERCA activity that include structure-derived thermodynamic information could permit *in silico* investigations of how disease-associated SERCA mutations,<sup>62,63</sup> post-translational modifications,<sup>64</sup> and binding of regulatory proteins such as phospholamban<sup>58</sup> affect pump function.

**3.3. Limitations.** There are several limitations of our approach that could be addressed in future studies. Our study largely focused on conformational changes and energetics of the cations' immediate coordination sphere.  $\text{Mg}^{2+}$  and  $\text{Ca}^{2+}$ -bound structures (PDB ID: 1su4 and 3w5b, respectively) deposited in the Protein Data Bank indicate substantial differences in the conformations of the transmembrane bundle helices and cytosolic domains that will necessarily contribute to the free energies of binding. For this reason, the free energy differences implied in experimental measurements of cation binding affinities reflect contributions from both ion coordination and the pump's different conformations. It is also important to emphasize that the MSA assumptions of a spherical binding volume within which amino acid oxygens are immobilized crudely approximates the actual binding site. Thus, the predicted thermodynamic quantities are most appropriate for rank-ordering different ion/binding site configurations. Additionally, there is evidence<sup>16,61</sup> that  $\text{Ca}^{2+}$  binding is cooperative, although here we treat the binding events independently. It may be possible to partially recover some of the cooperative behavior by modeling SERCA with

only one bound  $\text{Ca}^{2+}$  and using end-point methods such as Molecular Mechanics/Poisson–Boltzmann Surface Area (MM/PBSA)<sup>65</sup> to estimate energy changes upon binding a second  $\text{Ca}^{2+}$ . To our knowledge, however, a half-saturated  $\text{Ca}^{2+}$ -bound SERCA structure has not been determined, which would challenge efforts to validate predictions. Additionally, in the sequential binding model used by Inesi and others<sup>6,40</sup> ( $\text{E1} \rightarrow \text{E1.Ca} \rightarrow \text{E1'Ca} \rightarrow \text{E1'2Ca}$ ), the apparent kinetics governing the transition between the E1.Ca to E1'Ca states can vary depending on a variety of factors, including the presence of the regulatory protein phospholamban.<sup>58,66</sup> Thus, extending this model to broader conditions and regulatory proteins would require careful consideration of conformational changes that might accompany the E1.Ca to E1'Ca transition. Lastly, the  $\text{Ca}^{2+}$ -binding steps in our model are assumed to be in steady state relative to the substantially slower transitions between the E1 and E2 states. In the event that the pump is subject to rapid  $\text{Ca}^{2+}$  oscillations, such as spontaneous  $\text{Ca}^{2+}$  spiking in glia,<sup>67</sup> the steady-state approximation may be unreliable.

## 4. CONCLUSIONS

We utilized molecular dynamics simulations, mean sphere approximation theory, and state-based modeling to probe effects of  $\text{Ca}^{2+}$ ,  $\text{Mg}^{2+}$ , and  $\text{K}^{+}$  binding on the SERCA pump cycle. The MD and MSA approaches indicate that favorable binding of  $\text{Ca}^{2+}$  in the wild-type SERCA configuration is facilitated through a high degree of coordination by amino acids comprising the binding sites, as well as significant contributions from water coordination. This coordination pattern appears to be impaired in the E309Q and N796A variants; using MSA theory, we found that the chemical potential of  $\text{Ca}^{2+}$  binding is less favorable relative to wild-type as a result. Hence, mutations near the  $\text{Ca}^{2+}$  binding domains that alter the coordination number, hydration, and binding site volume can be expected to modulate  $\text{Ca}^{2+}$  affinity in a manner qualitatively described by the MSA theory. Similarly, the coordination patterns exhibited in the  $\text{Mg}^{2+}$ - and  $\text{K}^{+}$ -bound structures led to less favorable binding estimates from MSA theory. These findings were qualitatively consistent with measured affinity data reported in the literature.<sup>15–18,44,53</sup> Additionally, we developed a state-based model of SERCA activity that we used to (1) relate  $\text{Ca}^{2+}$  binding affinities to the SERCA pump rate and (2) determine whether  $\text{Mg}^{2+}$  and  $\text{K}^{+}$  are pump agonists or inhibitors. We found that the state model treating  $\text{Mg}^{2+}$  as an inhibitor and  $\text{K}^{+}$  as an agonist ( $\text{Mg}_i\text{K}_a$ ) was most consistent with experimental data. Despite the limitations of the assumptions used for the various models, we believe that the approach provides an attractive framework for evaluating allosteric functional effects of ion binding on SERCA, which may be extendable to other  $\text{Ca}^{2+}$  transporters, such as P2X4.<sup>68</sup>

## 5. METHODS

**5.1. Construction of the SERCA Systems.** Molecular dynamics (MD) simulations on wild-type (WT) SERCA and two variants of SERCA, E309Q and N796A, were performed; the latter variants were chosen given diminished site II  $\text{Ca}^{2+}$ -binding.<sup>43</sup> For the WT SERCA system, we considered apo (free of bound ions)  $\text{Ca}^{2+}$ -bound,  $\text{Mg}^{2+}$ -bound, and  $\text{K}^{+}$ -bound states.  $\text{Ca}^{2+}$ -bound (PDB ID: 1su4<sup>3</sup>) and  $\text{Mg}^{2+}$ -bound (E1.Mg, PDB ID: 3w5b<sup>48</sup>) SERCA X-ray crystal structures were used as

the starting structures. The apo SERCA system was constructed based on 1su4 with two  $\text{Ca}^{2+}$  ions removed as done in ref 69. The structure of the site I or II bound  $\text{K}^+$  SERCA has not been determined; thus, we created the structure based on the  $\text{Mg}^{2+}$ -bound variant. For the N796A variant,  $\text{Ca}^{2+}$ -bound and  $\text{Mg}^{2+}$ -bound cases were considered, based on mutating N796 to alanine. Similarly, for the E309Q variant, we obtained two rotamers compatible with the binding site as evaluated through UCSF Chimera.<sup>70</sup> These E309Q rotamers were designated as “E309Q\_r1” and “E309Q\_r2”. All SERCA cases considered in the present study are summarized in Table S1.

The cation coordinating acidic residues E309, E771, and D800 were assumed to be deprotonated, while E908 was protonated, consistent with ref 21. Further, a disulfide bond was introduced between residues C876 and C888. The system was inserted into a homogeneous 1-palmitoyl-2-oleoyl-*sn*-glycero-3-phosphocholine (POPC) lipid bilayer of POPC via the Membrane Builder<sup>71</sup> within the CHARMM-GUI software.<sup>72</sup> This system was solvated via TIP3P waters<sup>73</sup> using a 20 Å margin perpendicular to the membrane. Counterions  $\text{K}^+$  and chloride ( $\text{Cl}^-$ ) were added into the system via Monte Carlo method to neutralize the system and maintain an ionic strength of 0.15 M. Both the solvation and ion-adding were performed via the Solvator module within the CHARMM-GUI online server. The final system contained ~255 000 atoms including lipid bilayer with 461 lipids and ~59 000 TIP3P water molecules and was parametrized by the CHARMM36 force field.<sup>74,75</sup>

**5.2. Molecular Dynamics Simulations.** MD simulations were performed using NAMD.<sup>76</sup> The system was first subjected to an energy minimization process consisting of 2000 steps' steepest descent (SD) and 2000 steps' adopted basis Newton Raphson (ABNR) algorithm. For each case, the minimized system was heated from 0 to 303.14 K over 25 ps with 1 fs time step via the Langevin thermostat, using randomized velocities for three triplicate preparations. For each replica, harmonic constraints were introduced during minimization and heating on protein side chains, protein backbone atoms, lipid heavy atoms, and ions. The force constants of constraints were set to 5, 10, 10, and  $1.0 \times 10^1 \frac{\text{k}}{\text{mol \AA}^2}$ , respectively, and were gradually reduced to zero over five equilibration steps of 20 ps in duration. The 100 ns production simulations were then performed on the equilibrated system with the Shake algorithm,<sup>77</sup> using 2 fs timesteps.

**5.3. Simulation Trajectory Analysis.** Standard trajectory analyses including RMSF and coordination oxygen/ $\text{Ca}^{2+}$  distances were computed using Lightweight Object-Oriented Structure Library (LOOS).<sup>78</sup> Coordination pattern analysis on each cation with oxygen atoms from nearby amino acids were performed in each binding site. This consisted of extracting residues within 20 Å from D800 (the shared residue of the conventional two  $\text{Ca}^{2+}$ -binding sites in SERCA) based on the  $\text{Ca}^{2+}$ -bound SERCA crystal structure (PDB ID: 1su4). The water density around the cation was computed via the radial command implemented in CPPTRAJ<sup>79</sup> and analyzed via Grid Inhomogeneous Solvation Method (GIST) (as described in Section S1.4).

The MSA is a mean-field model which estimates cation chemical potentials in electrolyte solution with finite-sized ions. In this study, the SERCA cation binding sites were treated as confined filters filled with oxygens from coordinating

residues and water molecules. The MSA model calculates cation distributions among the bulk electrolyte solution that minimize the chemical potential for partitioning ions into a finite size volume occupied by coordinating oxygens; these volumes and numbers of oxygens were determined by MD as in Kucharski et al.<sup>34</sup> The free energy expression in this model assuming negatively charged spherical domains was based on a chemical potential accounting for electrostatic and hard-sphere interactions between ions inclusive of oxygens, as described in refs 35, 80, and 81. In this representation, which is analogous to the  $\text{Ca}^{2+}$  binding domain in  $\beta$ -PV and calcium channels,<sup>33–35</sup> ionic species that have a negative chemical potential in the binding filter are thermodynamically favored to bind. We include in this approach a solvation contribution as estimated via generalized Born theory of ion hydration energies:

$$\Delta G_{GB} = \frac{z^2}{r} \left( \frac{e^2 N_a}{2.4\pi\epsilon_0} \right) \left( 1 - \frac{1}{\epsilon_r} \right) \quad (4)$$

where  $z$  is charge number,  $r$  is radius,  $e$  is electron charge,  $N_a$  is the Avogadro constant, and  $\epsilon_0$  and  $\epsilon_r$  are vacuum dielectric and the relative dielectric constant of the solvent. Additional details are elaborated in the Supporting Information of ref 34.

In the SERCA system, the cation/SERCA configurations can present differing numbers of coordination oxygen atoms (see Figure 2 and Table S2) and volumes, as shown previously for  $\beta$ -PV in ref 34:

$$V_f = \frac{4}{3}\pi R^3 \quad (5)$$

$$R = r_{rdf} + r_{oxy} \quad (6)$$

where  $r_{rdf}$  is the radii of optimal coordination sphere which can be obtained from the cation–oxygen coordination pattern analysis based on MD simulations (see Figure 2) while  $r_{oxy}$  is the radius of the oxygen atom. Charges and radius values of all ions are taken from the Li–Merz work.<sup>82</sup> The specific parameters used in the MSA calculations are listed in Table S2.

#### 5.4. State-Based Model of the SERCA Pump Cycle.

SERCA pumping is characterized by two prominent states, E1 and E2, comprised of microstates corresponding to various conformations or bound states of the pump (Figure S4). In the E1 state, two  $\text{Ca}^{2+}$  ions bind to SERCA through a cooperative mechanism followed by the binding of  $\text{MgATP}$ .<sup>40</sup> We represent each state by an ordinary differential equation of the form

$$ds_i/dt = \sum k_{ji}s_j - \sum k_{ij}s_i \quad (7)$$

where  $s_i$  is state  $i$  and  $k_{ij}$  describe rates for transitioning between state  $i$  and state  $j$ . The models tested in this paper are summarized in Figure S4. While the cooperative  $\text{Ca}^{2+}$  binding mechanism in the E1 state is well-accepted, the  $\text{Ca}^{2+}$  release mechanism of the E2 state is not clearly resolved; therefore, we use the state representations proposed in Tran et al.<sup>41</sup>

On the basis of the technique proposed by Smith et al.,<sup>83</sup> we can apply the rapid equilibrium assumption to fast processes (those within E1 or E2) relative to the slow rates of transitions between the E1 and the E2 states to simplify the model. As shown in Figure S4, states in dashed boxes were assumed to be in quasi-steady state and thus were lumped together. Hence, the original multistate models were simplified into a two-state model (see bottom of Figure S4) in which new apparent rate

constants were derived based on original rate constants. The resulting equations are summarized in Section S1.3.

For the lumped two-state model, the turn over rate is derived as in Tran's paper:<sup>41</sup>

$$V = \frac{\alpha_1^+ \alpha_2^+ - \alpha_1^- \alpha_2^-}{\alpha_1^+ + \alpha_1^- + \alpha_2^+ + \alpha_2^-} \quad (8)$$

where  $\alpha_i^\pm$  are apparent rate constants between the lumped two states (the expressions are given in Section S1.3). The final parameters used are listed in Table S3.

## ■ ASSOCIATED CONTENT

### Supporting Information

The Supporting Information is available free of charge on the ACS Publications website at DOI: 10.1021/acs.jctc.8b01312.

Additional information regarding details of the method and supportive analysis (PDF)

## ■ AUTHOR INFORMATION

### Corresponding Author

\*E-mail: pkekeneshuskey@uky.edu (P. Kekeneshuskey).

### ORCID

Bin Sun: 0000-0003-2583-4493

### Funding

Research reported in this publication was supported by the Maximizing Investigators' Research Award (MIRA) (R35) from the National Institute of General Medical Sciences (NIGMS) of the National Institutes of Health (NIH) under Grant Number R35GM124977, as well as the Award 1F32HL114365-01A1. This work used the Extreme Science and Engineering Discovery Environment (XSEDE), which is supported by National Science Foundation under Grant Number ACI-1548562.

### Notes

The authors declare no competing financial interest.

## ■ ACKNOWLEDGMENTS

We thank Michael Autry for discussion of this work.

## ■ REFERENCES

- (1) Ma, H.; Inesi, G.; Toyoshima, C. Substrate-induced conformational fit and headpiece closure in the Ca<sup>2+</sup> ATPase (SERCA). *J. Biol. Chem.* **2003**, *278*, 28938–28943.
- (2) Inesi, G.; Prasad, A. M.; Pilankatta, R. The Ca<sup>2+</sup>ATPase of cardiac sarcoplasmic reticulum: Physiological role and relevance to diseases. *Biochem. Biophys. Res. Commun.* **2008**, *369*, 182–187.
- (3) Toyoshima, C.; Nakasako, M.; Nomura, H.; Ogawa, H. Crystal structure of the calcium pump of sarcoplasmic reticulum at 2.6 Å resolution. *Nature* **2000**, *405*, 647–655.
- (4) Toyoshima, C.; Nomura, H. Structural changes in the calcium pump accompanying the dissociation of calcium. *Nature* **2002**, *418*, 605–611.
- (5) Sørensen, T. L. M.; Clausen, J. D.; Jensen, A. M. L.; Vilsen, B.; Møller, J. V.; Andersen, J. P.; Nissen, P. Localization of a K<sup>+</sup>-binding site involved in dephosphorylation of the sarcoplasmic reticulum Ca<sup>2+</sup>-ATPase. *J. Biol. Chem.* **2004**, *279*, 46355–46358.
- (6) Olesen, C.; Picard, M.; Winther, A. M. L.; Gyru, C.; Morth, J. P.; Oxvig, C.; Møller, J. V.; Nissen, P. The structural basis of calcium transport by the calcium pump. *Nature* **2007**, *450*, 1036–1042.
- (7) Inesi, G.; Scarpa, A. Fast kinetics of adenosine triphosphate dependent Ca<sup>2+</sup> uptake by fragmented sarcoplasmic reticulum. *Biochemistry* **1972**, *11*, 356–359.
- (8) Froehlich, J. P.; Taylor, E. W. Transient state kinetic effects of calcium ion on sarcoplasmic reticulum adenosine triphosphatase. *J. Biol. Chem.* **1976**, *251*, 2307–2315.
- (9) Dupont, Y. Fluorescence studies of the sarcoplasmic reticulum calcium pump. *Biochem. Biophys. Res. Commun.* **1976**, *71*, 544–550.
- (10) Dupont, Y.; Leigh, J. B. Transient kinetics of sarcoplasmic reticulum Ca<sup>2+</sup>+Mg<sup>2+</sup> ATPase studied by fluorescence. *Nature* **1978**, *273*, 396–398.
- (11) Coan, C. R.; Inesi, G. Ca<sup>2+</sup>-dependent effect of acetylphosphate on spinlabeled sarcoplasmic reticulum. *Biochem. Biophys. Res. Commun.* **1976**, *71*, 1283–1288.
- (12) Meis, L.; Vianna, A. L. Energy Interconversion by the Ca<sup>2+</sup>-Dependent ATPase of the Sarcoplasmic Reticulum. *Annu. Rev. Biochem.* **1979**, *48*, 275–292.
- (13) Inesi, G. Mechanism of Calcium Transport. *Annu. Rev. Physiol.* **1985**, *47*, 573–601.
- (14) Mintz, E.; Guillain, F. Ca<sup>2+</sup> transport by the sarcoplasmic reticulum ATPase. *Biochim. Biophys. Acta, Bioenerg.* **1997**, *1318*, 52–70.
- (15) Clausen, J. D.; Bublitz, M.; Arnou, B.; Montigny, C.; Jaxel, C.; Møller, J. V.; Nissen, P.; Andersen, J. P.; Le Maire, M. SERCA mutant E309Q binds two Ca<sup>2+</sup> ions but adopts a catalytically incompetent conformation. *EMBO J.* **2013**, *32*, 3231–3243.
- (16) Inesi, G.; Kurzmack, M.; Coan, C.; Lewis, D. E. Cooperative calcium binding and ATPase activation in sarcoplasmic reticulum vesicles. *J. Biol. Chem.* **1980**, *255*, 3025–3031.
- (17) Guillain, F.; Gingold, M. P.; Champeil, P. Direct fluorescence measurements of Mg<sup>2+</sup> binding to sarcoplasmic reticulum ATPase. *J. Biol. Chem.* **1982**, *257*, 7366–7371.
- (18) Lee, a. G.; Baker, K.; Khan, Y. M.; East, J. M. Effects of K<sup>+</sup> on the binding of Ca<sup>2+</sup> to the Ca(2+)-ATPase of sarcoplasmic reticulum. *Biochem. J.* **1995**, *305*, 225–231.
- (19) Huang, Y.; Li, H.; Bu, Y. Molecular dynamics simulation exploration of cooperative migration mechanism of calcium ions in sarcoplasmic reticulum Ca<sup>2+</sup>-ATPase. *J. Comput. Chem.* **2009**, *30*, 2136–2145.
- (20) Kekeneshuskey, P. M.; Metzger, V. T.; Grant, B. J.; Andrew McCammon, J. Calcium binding and allosteric signaling mechanisms for the sarcoplasmic reticulum Ca<sup>2+</sup> ATPase. *Protein Sci.* **2012**, *21*, 1429–1443.
- (21) Espinoza-Fonseca, L. M.; Autry, J. M.; Thomas, D. D. Microsecond molecular dynamics simulations of Mg<sup>2+</sup>- And K<sup>+</sup>-Bound E1 intermediate states of the calcium pump. *PLoS One* **2014**, *9*, e95979.
- (22) Das, A.; Rui, H.; Nakamoto, R.; Roux, B. Conformational Transitions and Alternating-Access Mechanism in the Sarcoplasmic Reticulum Calcium Pump. *J. Mol. Biol.* **2017**, *429*, 647–666.
- (23) Rui, H.; Das, A.; Nakamoto, R.; Roux, B. Proton Counter-transport and Coupled Gating in the Sarcoplasmic Reticulum Calcium Pump. *J. Mol. Biol.* **2018**, *430*, S050–S065.
- (24) Fernández-De Gortari, E.; Espinoza-Fonseca, L. M. Structural basis for relief of phospholamban-mediated inhibition of the sarcoplasmic reticulum Ca<sup>2+</sup>-ATPase at saturating Ca<sup>2+</sup> conditions. *J. Biol. Chem.* **2018**, *293*, 12405–12414.
- (25) Ha, K. N.; Masterson, L. R.; Hou, Z.; Verardi, R.; Walsh, N.; Veglia, G.; Robia, S. L. Lethal Arg9Cys phospholamban mutation hinders Ca<sup>2+</sup>-ATPase regulation and phosphorylation by protein kinase A. *Proc. Natl. Acad. Sci. U. S. A.* **2011**, *108*, 2735–2740.
- (26) Bidwell, P.; Blackwell, D. J.; Hou, Z.; Zima, A. V.; Robia, S. L. Phospholamban binds with differential affinity to calcium pump conformers. *J. Biol. Chem.* **2011**, *286*, 35044–35050.
- (27) Smolin, N.; Robia, S. L. A structural mechanism for calcium transporter headpiece closure. *J. Phys. Chem. B* **2015**, *119*, 1407–1415.
- (28) Zhao, Y.; Ogawa, H.; Yonekura, S.-I.; Mitsuhashi, H.; Mitsuhashi, S.; Nishino, I.; Toyoshima, C.; Ishiura, S. Functional analysis of SERCALb, a highly expressed SERCA1 variant in myotonic dystrophy type 1 muscle. *Biochim. Biophys. Acta, Mol. Basis Dis.* **2015**, *1852*, 2042–2047.

- (29) Tadini-Buoninsegni, F.; Smeazzetto, S.; Gualdani, R.; Moncelli, M. R. Drug Interactions With the Ca<sup>2+</sup>-ATPase From Sarco(Endo)-Plasmic Reticulum (SERCA). *Front. Mol. Biosci.* **2018**, *5*, 36.
- (30) Dudev, T.; Lim, C. Competition among metal ions for protein binding sites: Determinants of metal ion selectivity in proteins. *Chem. Rev.* **2014**, *114*, 538–556.
- (31) Yu, H.; Noskov, S. Y.; Roux, B. Two mechanisms of ion selectivity in protein binding sites. *Proc. Natl. Acad. Sci. U. S. A.* **2010**, *107*, 20329–20334.
- (32) Kiyota, Y.; Takeda-Shitaka, M. Molecular recognition study on the binding of calcium to calbindin D9k based on 3D reference interaction site model theory. *J. Phys. Chem. B* **2014**, *118*, 11496–11503.
- (33) Nonner, W.; Gillespie, D.; Henderson, D.; Eisenberg, B. Ion accumulation in a biological calcium channel: Effects of solvent and confining pressure. *J. Phys. Chem. B* **2001**, *105*, 6427–6436.
- (34) Kucharski, A. N.; Scott, C. E.; Davis, J. P.; Kekenes-Huskey, P. M. Understanding Ion Binding Affinity and Selectivity in  $\alpha$ -Parvalbumin Using Molecular Dynamics and Mean Spherical Approximation Theory. *J. Phys. Chem. B* **2016**, *120*, 8617–8630.
- (35) Nonner, W.; Catacuzzeno, L.; Eisenberg, B. Binding and selectivity in L-type calcium channels: a mean spherical approximation. *Biophys. J.* **2000**, *79*, 1976–1992.
- (36) Gillespie, D.; Nonner, W.; Henderson, D.; Eisenberg, R. S. A physical mechanism for large-ion selectivity of ion channels. *Phys. Chem. Chem. Phys.* **2002**, *4*, 4763–4769.
- (37) Hughes, E.; Clayton, J. C.; Middleton, D. A. Cytoplasmic residues of phospholamban interact with membrane surfaces in the presence of SERCA: A new role for phospholipids in the regulation of cardiac calcium cycling? *Biochim. Biophys. Acta, Biomembr.* **2009**, *1788*, 559–566.
- (38) Israelachvili, J. N. *Intermolecular and Surface forces*; Academic Press: 2011.
- (39) Worley, J. F.; McIntyre, M. S.; Spencer, B.; Mertz, R. J.; Roe, M. W.; Dukes, I. D. Endoplasmic reticulum calcium store regulates membrane potential in mouse islet  $\beta$ -cells. *J. Biol. Chem.* **1994**, *269*, 14359–14362.
- (40) Cantilina, T.; Sagara, Y.; Inesi, G.; Jones, L. R. Comparative studies of cardiac and skeletal sarcoplasmic reticulum ATPases: Effect of a phospholamban antibody on enzyme activation by Ca<sup>2+</sup>. *J. Biol. Chem.* **1993**, *268*, 17018–17025.
- (41) Tran, K.; Smith, N. P.; Loiselle, D. S.; Crampin, E. J. A thermodynamic model of the cardiac sarcoplasmic/endoplasmic Ca<sup>2+</sup>(SERCA) pump. *Biophys. J.* **2009**, *96*, 2029–2042.
- (42) Berridge, M. J.; Bootman, M. D.; Roderick, H. L. Calcium signalling: dynamics, homeostasis and remodelling. *Nat. Rev. Mol. Cell Biol.* **2003**, *4*, 517–529.
- (43) Clarke, D. M.; Loo, T. W.; Inesi, G.; MacLennan, D. H. Location of high affinity Ca<sup>2+</sup> - binding sites within the predicted transmembrane domain of the sarco-plasmic reticulum Ca<sup>2+</sup>-ATPase. *Nature* **1989**, *339*, 476–478.
- (44) Inesi, G.; Zhang, Z.; Lewis, D. Cooperative setting for long-range linkage of Ca<sup>2+</sup>-binding and ATP synthesis in the Ca<sup>2+</sup>-ATPase. *Biophys. J.* **2002**, *83*, 2327–2332.
- (45) Inesi, G.; Ma, H.; Lewis, D.; Xu, C. Ca<sup>2+</sup> occlusion and gating function of Glu309 in the ADP-fluoroaluminate analog of the Ca<sup>2+</sup>-ATPase phosphoenzyme intermediate. *J. Biol. Chem.* **2004**, *279*, 31629–31637.
- (46) Shigekawa, M.; Pearl, L. J. Activation of calcium transport in skeletal muscle sarcoplasmic reticulum by monovalent cations. *J. Biol. Chem.* **1976**, *251*, 6947–6952.
- (47) Vianna, A. L. Interaction of calcium and magnesium in activating and inhibiting the nucleoside triphosphatase of sarcoplasmic reticulum vesicles. *Biochim. Biophys. Acta, Enzymol.* **1975**, *410*, 389–406.
- (48) Toyoshima, C.; Iwasawa, S.; Ogawa, H.; Hirata, A.; Tsueda, J.; Inesi, G. Crystal structures of the calcium pump and sarcolipin in the Mg<sup>2+</sup>-bound E1 state. *Nature* **2013**, *495*, 260–264.
- (49) Jones, L. R. Mg<sup>2+</sup>-and ATP effects on K<sup>+</sup>-activation of the Ca<sup>2+</sup>-transport ATPase of cardiac sarcoplasmic reticulum. *Biochim. Biophys. Acta, Biomembr.* **1979**, *557*, 230–242.
- (50) Shannon, R. D.; Prewitt, C. T. Effective ionic radii in oxides and fluorides. *Acta Crystallogr., Sect. B: Struct. Crystallogr. Cryst. Chem.* **1969**, *25*, 925–946.
- (51) Cordero-Morales, J. F.; Cuello, L. G.; Zhao, Y.; Jogini, V.; Cortes, D. M.; Roux, B.; Perozo, E. Molecular determinants of gating at the potassium channel selectivity filter. *Nat. Struct. Mol. Biol.* **2006**, *13*, 311–318.
- (52) Yamasaki, K.; Wang, G.; Daiho, T.; Danko, S.; Suzuki, H. Roles of Tyr122- hydrophobic cluster and K<sup>+</sup>-binding in Ca<sup>2+</sup>-releasing process of ADP-insensitive phosphoenzyme of sarcoplasmic reticulum Ca<sup>2+</sup>-ATPase. *J. Biol. Chem.* **2008**, *283*, 29144–29155.
- (53) Moutin, M. J.; Dupont, Y. Interaction of potassium and magnesium with the high affinity calcium-binding sites of the sarcoplasmic reticulum calcium-ATPase. *J. Biol. Chem.* **1991**, *266*, 5580–5586.
- (54) Musgaard, M.; Thøgersen, L.; Schiøtt, B. Protonation states of important acidic residues in the central Ca<sup>2+</sup> ion binding sites of the Ca<sup>2+</sup>-ATPase: A molecular modeling study. *Biochemistry* **2011**, *50*, 11109–11120.
- (55) Sipido, K. R.; Wier, W. G. Flux of Ca<sup>2+</sup> across the sarcoplasmic reticulum of guinea pig cardiac cells during excitation contraction coupling. *J. Physiol. (Oxford, U. K.)* **1991**, *435*, 605–630.
- (56) Luo, C. H.; Rudy, Y. A dynamic model of the cardiac ventricular action potential: I. Simulations of ionic currents and concentration changes. *Circ. Res.* **1994**, *74*, 1071–1096.
- (57) Shannon, T. R.; Wang, F.; Puglisi, J.; Weber, C.; Bers, D. M. A mathematical treatment of integrated Ca dynamics within the ventricular myocyte. *Biophys. J.* **2004**, *87*, 3351–3371.
- (58) Ceholski, D. K.; Trieber, C. A.; Holmes, C. F. B.; Young, H. S. Lethal, hereditary mutants of phospholamban elude phosphorylation by protein kinase A. *J. Biol. Chem.* **2012**, *287*, 26596.
- (59) Higgins, E. R.; Cannell, M. B.; Sneyd, J. A buffering SERCA pump in models of calcium dynamics. *Biophys. J.* **2006**, *91*, 151–163.
- (60) Koivumäki, J. T.; Takalo, J.; Korhonen, T.; Tavi, P.; Weckström, M. Modelling sarcoplasmic reticulum calcium ATPase and its regulation in cardiac myocytes. *Philos. Trans. R. Soc., A* **2009**, *367*, 2181–2202.
- (61) Zhang, Z.; Lewis, D.; Strock, C.; Inesi, G.; Nakasako, M.; Nomura, H.; Toyoshima, C. Detailed characterization of the cooperative mechanism of Ca<sup>2+</sup> binding and catalytic activation in the Ca<sup>2+</sup> transport (SERCA) ATPase. *Biochemistry* **2000**, *39*, 8758–8767.
- (62) Dhitavat, J.; Dode, L.; Leslie, N.; Sakuntabhai, A.; Lorette, G.; Hovnanian, A. Mutations in the sarcoplasmic/endoplasmic reticulum Ca<sup>2+</sup> ATPase isoform cause Darier's disease. *J. Invest. Dermatol.* **2003**, *121*, 486–489.
- (63) Hovnanian, A. SERCA pumps and human diseases. *Subcell. Biochem.* **2007**, *45*, 337–363.
- (64) Xu, A.; Hawkins, C.; Narayanan, N. Phosphorylation and activation of the Ca(2+)-pumping ATPase of cardiac sarcoplasmic reticulum by Ca<sup>2+</sup>/calmodulin-dependent protein kinase. *J. Biol. Chem.* **1993**, *268*, 8394–8397.
- (65) Kollman, P. A.; Massova, I.; Reyes, C.; Kuhn, B.; Huo, S.; Chong, L.; Lee, M.; Lee, T.; Duan, Y.; Wang, W.; Donini, O.; Cieplak, P.; Srinivasan, J.; Case, D. A.; Cheatham, T. E. Calculating Structures and Free Energies of Complex Molecules: Combining Molecular Mechanics and Continuum Models. *Acc. Chem. Res.* **2000**, *33*, 889–897.
- (66) Glaves, J. P.; Trieber, C. A.; Ceholski, D. K.; Stokes, D. L.; Young, H. S. Phosphorylation and mutation of phospholamban alter physical interactions with the sarcoplasmic reticulum calcium pump. *J. Mol. Biol.* **2011**, *405*, 707–723.
- (67) Schipke, C. G.; Heidemann, A.; Skupin, A.; Peters, O.; Falcke, M.; Kettenmann, H. Temperature and nitric oxide control spontaneous calcium transients in astrocytes. *Cell Calcium* **2008**, *43*, 285–295.

- (68) Chun, B. J.; Stewart, B. D.; Vaughan, D. D.; Bachstetter, A. D.; Kekenes-Huskey, P. M. Simulation of P2X-mediated calcium signalling in microglia. *J. Physiol. (Oxford, U. K.)* **2019**, *597*, 799–818.
- (69) Espinoza-Fonseca, L. M.; Thomas, D. D. Atomic-level characterization of the activation mechanism of serca by calcium. *PLoS One* **2011**, *6*, e26936.
- (70) Pettersen, E. F.; Goddard, T. D.; Huang, C. C.; Couch, G. S.; Greenblatt, D. M.; Meng, E. C.; Ferrin, T. E. UCSF Chimera A visualization system for exploratory research and analysis. *J. Comput. Chem.* **2004**, *25*, 1605–1612.
- (71) Wu, E. L.; Cheng, X.; Jo, S.; Rui, H.; Song, K. C.; Dávila-Contreras, E. M.; Qi, Y.; Lee, J.; Monje-Galvan, V.; Venable, R. M.; Klauda, J. B.; Im, W. CHARMM-GUI Membrane Builder toward realistic biological membrane simulations. *J. Comput. Chem.* **2014**, *35*, 1997–2004.
- (72) Jo, S.; Kim, T.; Iyer, V. G.; Im, W. CHARMM-GUI: A web-based graphical user interface for CHARMM. *J. Comput. Chem.* **2008**, *29*, 1859–1865.
- (73) Jorgensen, W. L.; Chandrasekhar, J.; Madura, J. D.; Impey, R. W.; Klein, M. L. Comparison of simple potential functions for simulating liquid water. *J. Chem. Phys.* **1983**, *79*, 926–935.
- (74) MacKerell, A. D.; et al. All-Atom Empirical Potential for Molecular Modeling and Dynamics Studies of Proteins. *J. Phys. Chem. B* **1998**, *102*, 3586–3616.
- (75) MacKerell, A. D.; Feig, M.; Brooks, C. L. Improved Treatment of the Protein Backbone in Empirical Force Fields. *J. Am. Chem. Soc.* **2004**, *126*, 698–699.
- (76) Phillips, J. C.; Braun, R.; Wang, W.; Gumbart, J.; Tajkhorshid, E.; Villa, E.; Chipot, C.; Skeel, R. D.; Kalé, L.; Schulten, K. Scalable molecular dynamics with NAMD. *J. Comput. Chem.* **2005**, *26*, 1781–1802.
- (77) Ryckaert, J.-P.; Ciccotti, G.; Berendsen, H. J. Numerical integration of the cartesian equations of motion of a system with constraints: molecular dynamics of n-alkanes. *J. Comput. Phys.* **1977**, *23*, 327–341.
- (78) Romo, T. D.; Leioatts, N.; Grossfield, A. Lightweight Object Oriented Structure analysis: Tools for building Tools to Analyze Molecular Dynamics Simulations. *J. Comput. Chem.* **2014**, *35*, 2305–2318.
- (79) Roe, D. R.; Cheatham, T. E. PTRAJ and CPPTRAJ: Software for Processing and Analysis of Molecular Dynamics Trajectory Data. *J. Chem. Theory Comput.* **2013**, *9*, 3084–3095.
- (80) Høye, J. S.; Blum, L. The mean spherical model for asymmetric electrolytes: Thermodynamics and the pair correlation function. *Mol. Phys.* **1978**, *35*, 299–300.
- (81) Herrera, J. N.; Blum, L. Sticky electrolyte mixtures in the Percus Yevick- /mean spherical approximation. *J. Chem. Phys.* **1991**, *94*, 5077–5082.
- (82) Li, P.; Roberts, B. P.; Chakravorty, D. K.; Merz, K. M. Rational Design of Particle Mesh Ewald Compatible Lennard-Jones Parameters for + 2 Metal Cations in Explicit Solvent. *J. Chem. Theory Comput.* **2013**, *9*, 2733–2748.
- (83) Smith, N.; Crampin, E. Development of models of active ion transport for whole-cell modelling: cardiac sodium potassium pump as a case study. *Prog. Biophys. Mol. Biol.* **2004**, *85*, 387–405.